Constructing efficient solar light photocatalytic system with Ag-introduced carbon nitride for organic pollutant elimination

Xi Wu[a], Changhai Lu[a], Jingjie Liu[a], Shaoqing Song[a,*], Chuanzhi Sun[b,*]

[a] State key Laboratory Breeding Base of Nuclear Resources and Environment, East China University of Technology, Nanchang 330013, PR China
[b] College of Chemistry, Chemical Engineering and Materials Science, Shandong Normal University, Jinan 250014, PR China

ARTICLE INFO

ABSTRACT

Owing to the unique electronic and optical properties, carbon nitride (CN) materials have attracted widespread interest for photocatalytic application in the field of environment and energy. However, low carrier mobility and insufficient sunlight absorption limit the efficient application, which is attributed to the planar hydrogen bonding between strands of polymeric melon units with NH/NH_2. Herein, Ag-introduced CN (AgCN) samples were designed as photocatalysts by introducing Ag into CN to weaken the planar hydrogen bonding for photocatalytically eliminating methyl orange pollutant. Spectroscopy, electrochemistry and computational studies revealed that AgCN photocatalyts presented a significantly enhanced sunlight absorption, efficient carrier mobility as well as improved O_2 adsorption state. As a result, photoreactivity for methyl orange photooxidation elimination over AgCN was significantly enhanced, with apparent rate of $0.13 \, min^{-1}$ for optimal AgCN-4 under visible-light irradiation, which was 6.50, 8.13, 2.60, and 4.33 times that of Bi_2WO_6, $BiOCl$, Ag/CN, and Ag_2CO_3, respectively. The result supplied an efficient approach for constructing effective visible-light-irradiation photocatalysts for environmental purification.

© 2017 Elsevier B.V. All rights reserved.

1. Introduction

With energy crisis and continued deterioration of global environment, semiconductor photocatalysis technology has drawn great attention and been proposed as a"green"strategy for pollutants elimination, H_2 evolution from H_2O dissociation, and CO_2 photoreduction into hydrocarbons [1–7]. It is known that the main steps in photocatalysis process include: (i) generation of charges through photon absorption of photocatalysts; (ii) timely transfer of photogenerated electrons from hole location; (iii) photocatalytic redox reaction on photocatalyst surface [8,9]. However, for the explored TiO_2, WO_3, ZnO, and ZnS, photogenerated charges can not be effectively transferred, thus leading a poor photocatalytic performance. Moreover, the relatively inefficient utilization of solar energy (only 4% of solar spectrum) limits the further application. From the photocatalysis process, we can see that light absorption and electron transfer efficiency play a key role in the subsequent photocatalytic reaction [10,11]. Theoretically, graphene has been considered as the optimal photocatalytic material due to good light absorption capability and outstanding electron transport property.

However, there are hydrogen bonds between carboxl and hydroxyl groups on the actual graphene (e.g., oxidized graphene or reduced oxidized graphene), and thus these graphenes are still subject to UV light responsiveness [12,13]. Meanwhile, series of visible-light-driven semiconductors have been explored, such as Bi_2WO_6, Fe_2O_3, Ag_3PO_4, $BiOX$ (X = Cl, Br, I), and these photocatalytic materials continue to promote the development of photocatalysis in the field of environment and energy [14–31].

Graphitic carbon nitride (CN), a polymer of tri-s-triazine with π-conjugated characteristic with a bandgap of 2.7 eV, possesses high thermal, chemical stability as well as ability of absorbing visible light with wavelength up to around 450 nm, which make the material to be promising photocatalyst for photocatalysis applications [32–43]. Actually, low carrier mobility and insufficient sunlight absorption limit the energy conversion efficiency [40,44]. Results reveal that the CN composed by tri-s-triazine rings shows strong covalent C—N bonds in each layer and weak van der Waals force between layers, and thus a large amount of planar hydrogen bonding is formed between strands of polymeric melon units with —NH/NH_2 due to the larger electronegativity of N (χ(N) = 3.04, ion radius r(N^{3-}) = 0.171 Å) [45,46]. The existence of hydrogen bonds in the covalent carbon nitride framework may block electron conduction across the plane and leads to low conductivity [43,47]. In principle, carrier mobility and sun-

Fig. 1. TEM images for AgCN-1 (A), AgCN-2 (B), AgCN-3 (C) and AgCN-4 (D).

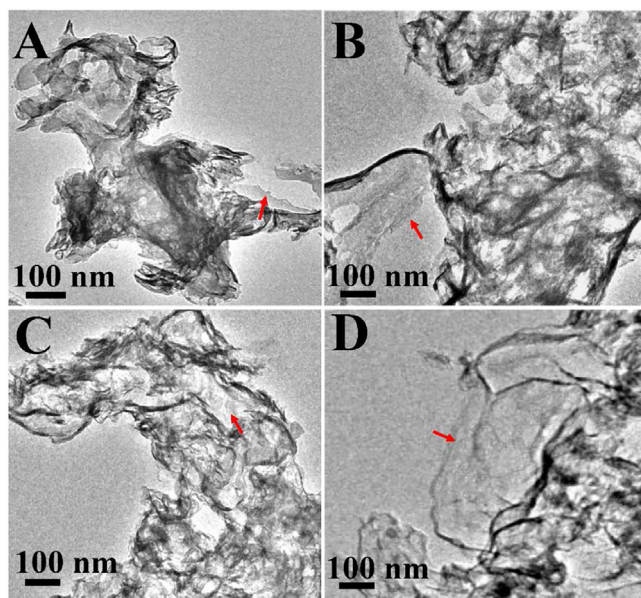**Fig. 2.** XRD patterns of AgCN-1, AgCN-2, AgCN-3 and AgCN-4.

light absorption of CN can be improved by weakening the planar hydrogen bonding, therefore, the element with low electronegativity and suitable radius is used to partially replace N of CN, e.g., B (χ(B) = 2.04, r(B^{3+}) = 0.26 Å), P (χ(P) = 2.19, r(P^{3-}) = 0.212 Å), and even metal Fe (r(Fe^{3+}) = 0.064 Å), Ni (r(Ni^{2+}) = 0.072 Å), K (r(K$^+$) = 0.133 Å)[48–52]. Ag atom can not only possess the low electronegativity (χ(Ag) = 1.93, r(Ag$^+$) = 0.126 Å), but also show good ability to accept and transfer carriers. Intuitively, Ag will be introduced into the polymeric melon units of CN, which can weaken the hydrogen bonding of CN and theoretically promote the effective utilization of photogenerated charges. Herein, Ag was introduced into CN (AgCN) for the photocatalytic elimination of methyl orange pollutant, and the designed AgCN was investigated by spectroscopy characterizations and theoretical calculation. The remarkable carrier mobility and sunlight absorption of AgCN have been achieved due to the weakened hydrogen bonds by the introduction of Ag, which exhibited high photocatalytic activity for the elimination of methyl orange under visible-light irradiation.
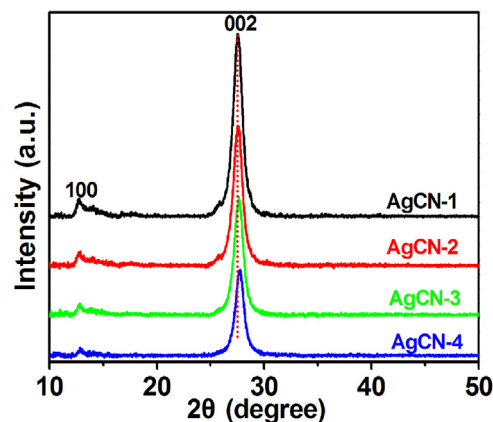
2. Experimental

2.1. Photocatalysts preparation

In the preparation process, AgCN samples were prepared through heating the mixture of urea and AgNO$_3$ under the Ar atmosphere. In detail, urea and AgNO$_3$ were firstly dissolved in deionized water and then agitated for 1 h. Afterwards, the resulting mixture was dried in a vacuum at 60 °C for 2 h, and subsequently placed in the quartz tube of a horizontal furnace. The temperature was then ramped at 5 °C min^{-1} up to 540 °C in Ar flow and kept for 2 h. After that, the reactor was spontaneously cooled down to room temperature under Ar as protective ambient. The resulting products were referred to as AgCN-1, AgCN-2, AgCN-3, and AgCN-4 when the mass ratio of urea and AgNO$_3$ is 10/0.005, 10/0.015, 10/0.025, and 10/0.035, respectively. Moreover, CN sample was synthesized by directly heating 10 g urea in a horizontal furnace for comparison.

2.2. Characterization

The morphology was observed with using transmission electron microscope (TEM, JEM-2100F). The chemical component was investigated by X-ray diffraction (XRD, Rigaku RINT-2000 instrument using Cu Kα radiation (40 kV) with a scanning rate of 0.067°/s). The chemical state was performed with X-ray photo-
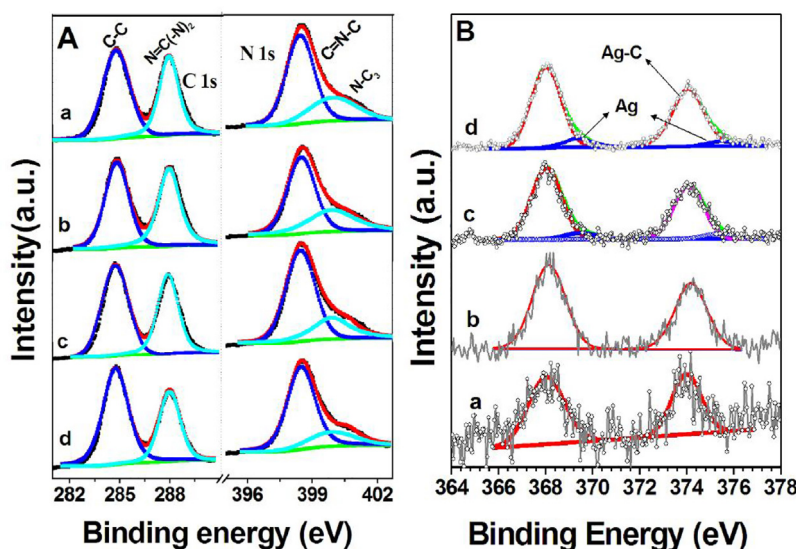

Fig. 3. High-resolution XPS spectra of C1s, N 1 s (A) and Ag 3d (B) for AgCN samples.

electron spectroscopy (XPS, ultra-high-vacuum VG ESCALAB 210 electron spectrometer). The binding energies of XPS spectra refer to C 1s at 284.6 eV. UV–vis diffuse reflection spectra were conducted by UV–vis spectrophotometer (UV-2550, Shimadzu, Japan). Steady fluorescence emission spectra were recorded at room temperature with a Steady State Spectrometer (Edinburgh Instruments, FLSP-920). Photocurrent test was performed on CHI 660D electrochemical workstation. Three electrode measurement system was constructed in 1 M Na_2SO_4 aqueous solution by intermittent illumination at 0.5 V. LED (3 W, 365 nm) was utilized as irradiation light with intensity of 80.0 mW cm^{-2}. O_2 stripping of CN and AgCN on saturated calomel electrode (SCE) was carried out in 0.1 M NaOH solution. O_2 (99.99%) and N_2 (99.999%) were purged into NaOH solution for 45 and 30 min, respectively. The residual O_2 in the solution was eliminated by bubbling N_2 for 60 min. O_2 stripping CV scans were performed with 5 mV s^{-1} scan rate.

2.3. Photocatalytic tests

AgCN photocatalysts were utilized to photocatalytically eliminate MO pollutant under visible-light irradiation at ambient temperature. The specific photocatalytic process follows the steps, 50 mg photocatalyst was added into 25 mL of methyl orange solution (10 mg/L) and subsequently experienced an adsorption-desorption equilibrium procedure. Afterwards, a 350 W xenon lamp with a 400 nm optical filter was utilized as a light irradiation system. Methyl orange concentration was detected by UV–vis spectrophotometer (UV-1240, SHIMADZU, Japan). After illumination, a certain amount of solution mixture was drawn off and centrifuged to ensure the concentration variety of methyl orange at certain time intervals.

To reveal the photocatalytic essence of MO elimination, triethanolamine (TEOA, 0.01 M), p-benzoquinone (BZQ, 0.001 M), and isopropanol (IPA, 0.02 M) were used as trapping agent to investiga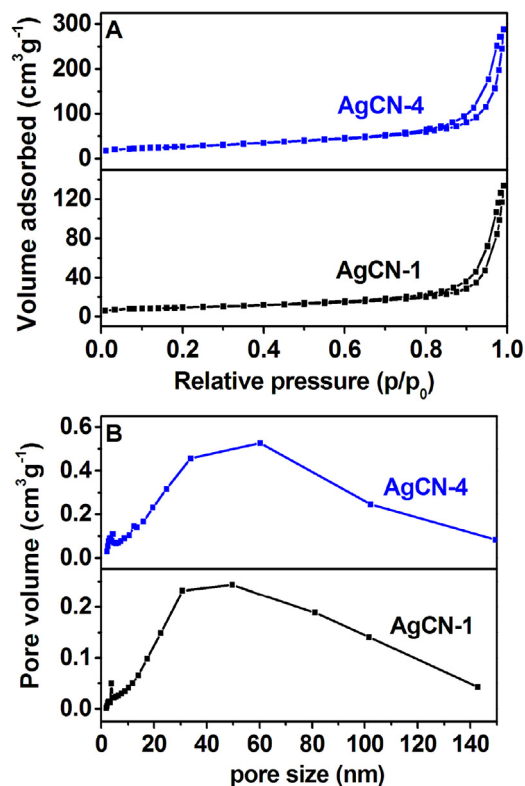te effect of photogenerated holes (h$^+$), superoxide anion radicals (O$_2^-$) and hydroxyl radicals (·OH), respectively.

Fig. 4. N_2 adsorption-desorption isotherms of AgCN-1 and AgCN-4 samples (A), and the corresponding pore size distribution curves (B).
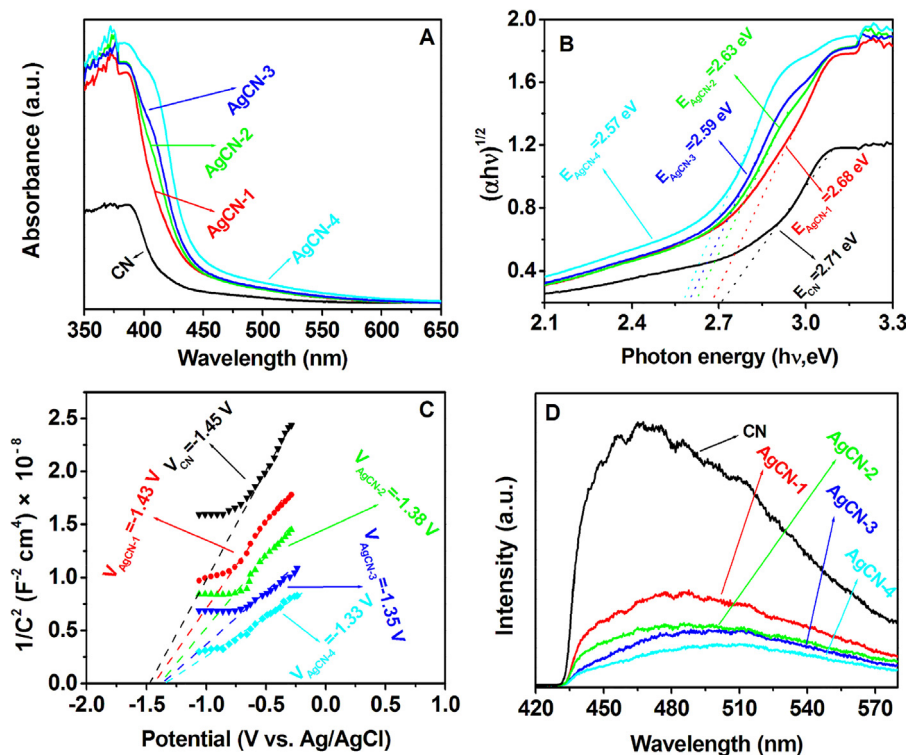
Fig. 5. (A) Optical absorption spectra of CN and AgCN samples; (B) Plots of $(\alpha h\upsilon)^{1/2}$ vs. photon energy (hυ), (C) Electrochemical Mott-Schottky plots of CN and AgCN samples, and (D) Photoluminescence spectra of CN and AgCN.
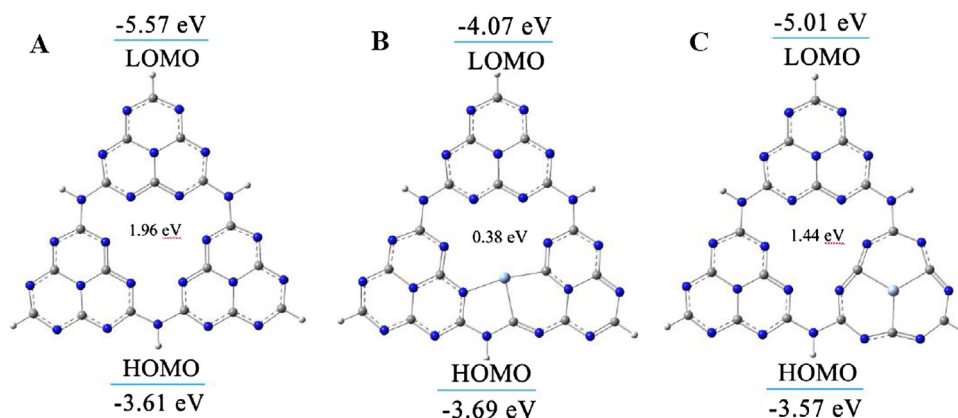
Fig. 6. Molecular orbital energies and structures of the CN (A) and AgCN with substitutional Ag for N of site 1 (B), and site 2 (C). Gray: C, blue: N and light blue: Ag.
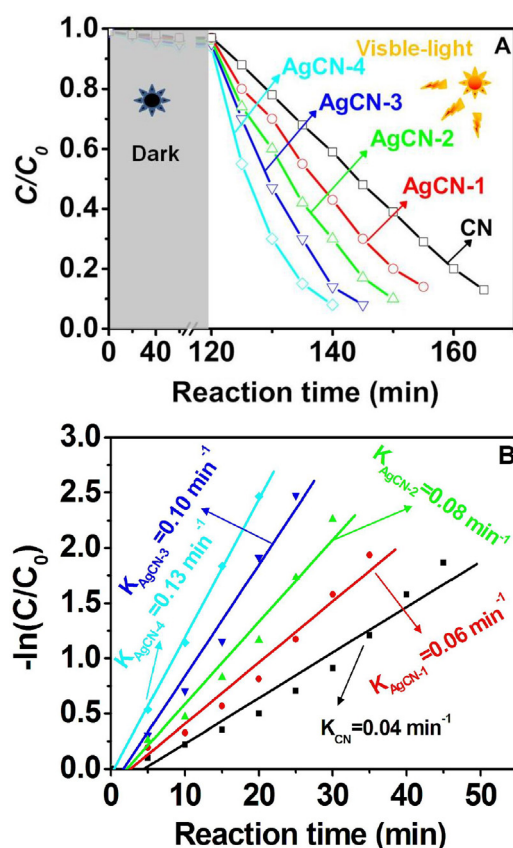

Fig. 7. Variation of MO concentration vs. reaction time using AgCN and CN as photocatalysts; and (B) Pseudo-first-order kinetics modeling of MO photoelimination over these samples.

2.4. Computational details

All calculations were performed with the Gaussian 09 suite of computational programs. DFT calculations were conducted at the PBE/6-31G*(C, H, N and S)/LanL2DZ(U) level to probe the electronic structures and O_2 adsorption state of the CN and AgCN. The modes of CN and AgCN were constructed by a truncated unit with three melems, in which two possible sites of nitrogen substituted by Ag were considered.

3. Results and discussion

3.1. Morphology and composition of the AgCN photocatalysts

The morphology of the as-prepared AgCN samples were investigated by TEM, and the results were shown in Fig. 1. From Fig. 1A, the layered nanosheets with some irregular pores were accumulated, and we can also see that the edge of nanosheet shows relative structural integrity for AgCN-1; with increasing the introduction content of Ag, the pores apparently disappeared, the large complete nanosheet can be obtained for AgCN-2, AgCN-3 & AgCN-4. FESEM and corresponding elemental mapping of AgCN samples (AgCN-4 as the representative) were performed to investigate the distribution patterns of the component elements. As shown in Fig. S1 of Supplementary material, C, N and Ag elements are uniformly distributed in the AgCN samples. The results confirmed that the introduction of Ag can construct the integrity framework of AgCN by weakening hydrogen bond [46]. The obtained large complete nanosheet is beneficial to the photocatalytic reaction, because the photogenerated electrons can conveniently transfer with absorbing the small amount of light energy [53].

The XRD characterization of AgCN samples was shown in Fig. 2. The peaks at 13.1° for these prepared samples arise from the (100) plane of aromatic lattice packing [54–56]. The (002) peaks stem from the periodic stacking of layers in the graphitic structure [46], and it is seen that the (002) peak is slightly shifted from 27.5° to 27.7° with increasing introduction content of Ag. Moreover, the overall weakened intensity of AgCN is confirmed due to the introduction of Ag into tri-s-triazine rings. Results show that the formed bond lengths between Ag, C, and N are different due to their distinct ionic radius, which therefore leads to a decrease intensity of crystalline [50]. The surface compositions and chemical states of AgCN were further investigated by XPS (Fig. 3). C 1s spectrum at 284.6 and 288.0 eV can be ascribed to the standard reference carbon and the sp^2 bonded C in the N=C—N (Fig. 3A), respectively [51,57,58]. N 1s spectrum was considered to be composed by N species of C=N—C (398.8 eV), and C_3–N (399.6 eV) [58,59]. Ag 3d5/2 and Ag 3d3/2 peaks were located at 368.1 and 374.2 eV, each Ag 2p spectrum can be fitted into the dominant peak at 368.1 and 374.2 eV assigned to the C–Ag bond, and the weak peak at 369.5 and 375.5 eV corresponded to Ag metal [60,61]. In order to further ensure the C-Ag species, the prepared AgCN-4 was treated with H_2 and characterized with XPS (Fig. S2 of Supplementary material), nevertherless, we have not seen the increase of content for Ag metal species, and the intensity of peaks at around 368 and 374 eV show the similar with original AgCN-4, which can further confirm the formation of Ag-C species. According to the element content detected by XPS
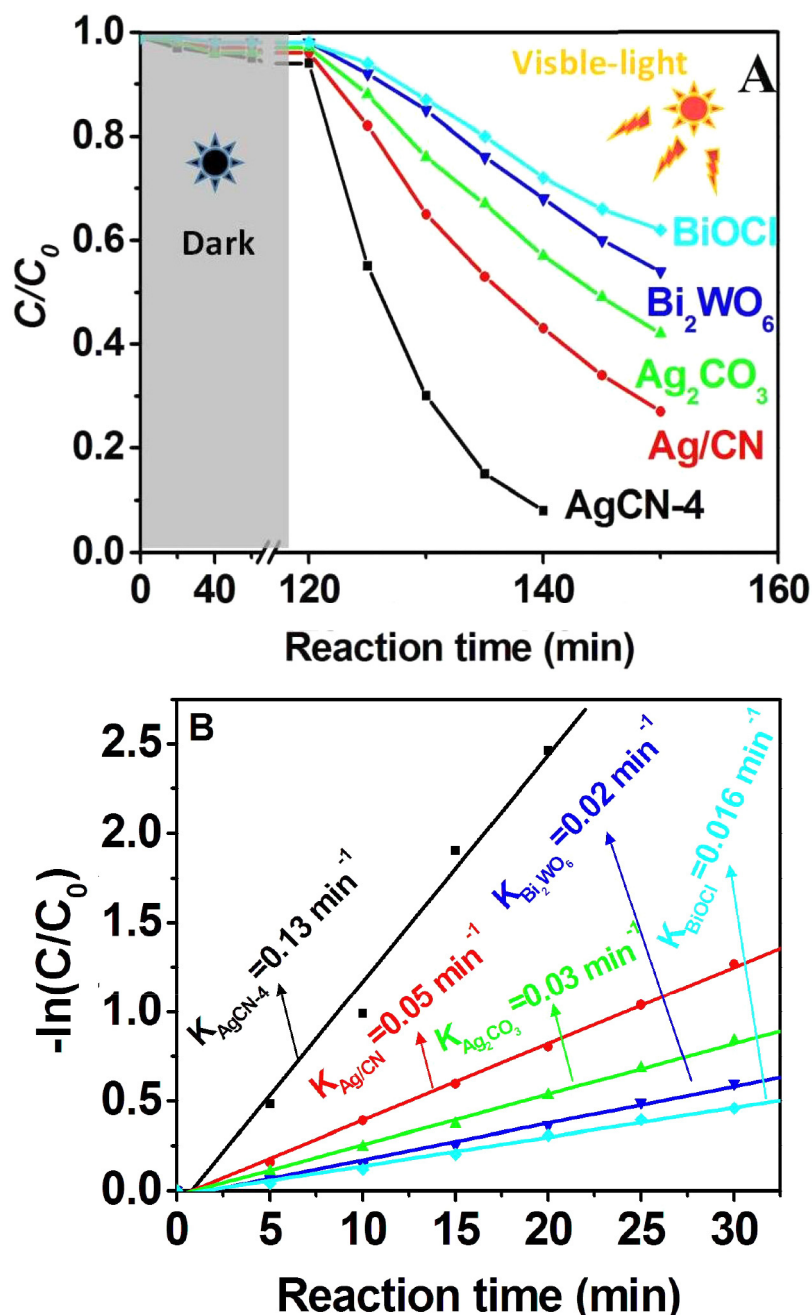
Fig. 8. The variation of MO concentration vs. illumination time (A) and pseudo-first-order rate constant (k) of MO elimination (B) over photocatalysts.

and each deconvoluted spectrum peak area of Ag species, we can see that Ag replaced N of CN, which thus formed the C-Ag species [52]; plasmonics Ag can only be detected in the AgCN-3 and AgCN-4 (Table S1 of Supplementary material); the Ag-C content increased from 0.11 to 0.54, and plasmonics Ag content of AgCN-3 and AgCN-4 is 0.025, and 0.06, respectively. From the starting point for material design, introduction of Ag into the structure of CN can be achieved, which will weaken the planar hydrogen bonding of CN. In principle, the Ag-C structure and plasmonics Ag species will influence the carrier mobility and sunlight absorption of AgCN.

The specific surface areas and porous characteristic of AgCN sampes were investigated by N_2 adsorption/desorption isotherms and pore-size distributions. In Fig. 4A, the adsorption isotherms show the type IV with obvious H3-type hysteresis loops from $P/P_0 = 0.85$ to 1, indicating the formation of slitlike mesoporous with stacking of nanosheets. Pore structure analysis show that the

sizes are mainly in the range of 5–52 nm (Fig. 4B). BET specific surface areas are 31.5, 55.8, 67.3, and 91.5 m^2/g corresponding to AgCN-1, AgCN-2, AgCN-3, and AgCN-4, respectively. The gradually increased surface area of PC_3N_4 samples will facilitate pollutant adsorption and thus promote the photocatalytic elimination reaction.

3.2. Electronic structure of AgCN photocatalysts

The electronic structure of AgCN was revealed by UV–vis absorption spectroscopy and theoretical calculation. As seen in Fig. 5A, the absorption edges of the AgCN samples ranged from 443 to 456 nm compared with that of CN at 428 nm. The red shift of the absorption, as well as the high absorption intensity in the ultraviolet region, suggested that AgCN samples can trap more solar energy to generate more electron-hole pairs under the solar [54,62]. Moreover,
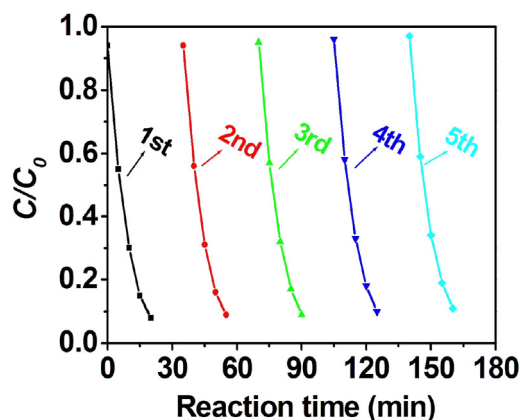
Fig. 9. Cycling runs of AgCN-4 for the photocatalytic elimination of MO pollutant.

Fig. 10. Transient photocurrent responses of CN and AgCN-4 photocatalysts in 1 M Na_2SO_4 aqueous solution under visible-light irradiation at 0.5 V vs. Ag/AgCl.

it can be seen that the LSPR peak of Ag at 410 nm was presented for AgCN-3 and AgCN-4, however it is comparatively weak, which thus could not change the intrinsic band gap of AgCN. From the plots of Kubelka-Munk function versus the energy of the absorbed light, the calculated intrinsic band energy was 2.71, 2.68, 2.63, 2.59, and 2.57 eV corresponding to CN, AgCN-1, AgCN-2, AgCN-3, and AgCN-4, respectively (Fig. 5B). To further investigate the electronic structure characteristic of AgCN samples, AgCN samples were deposited on the FTO substrate, which can determine the CB and VB potentials of the AgCN samples by electrochemical impedance spectroscopic analysis along with Mott-Schottky method, as shown in Fig. 5C. We can see that the positive slop of the straight lines present the *n*-type conductivity of AgCN samples, and the intercept on the abscissa was used to calculate the CB potentials. As presented in Fig. 5C, the CB potentials are −1.45, −1.43, −1.38, −1.35, and −1.33 V (vs. Ag/AgCl), i.e., −1.22, −1.20, −1.15, −1.12, and −1.10 V (vs. SHE at pH = 7) for CN, AgCN-1, AgCN-2, AgCN-3, and AgCN-4, respectively. The VB potential can be determined by $E_{CB} = E_{VB} − E_g$, and VB potentials of the samples was calculated to be 1.49 (CN), 1.48 (AgCN-1), 1.48 (AgCN-2), 1.47 (AgCN-3), and 1.47 V (AgCN-4) vs. SHE. In Fig. 5D, AgCN samples give a similar band-to-band fluorescence emission characteristic as CN. The evidenced shift of intrinsic fluorescence emission peak from to nm by Ag introduction reveals the narrowed bandgap of AgCN, which accorded with that of UV–vis absorption spectroscopy. Although a slight downshift in the conduction band for AgCN may cause the lower reduction ability of electron, its narrow band gap and enhanced light absorption could improve the activity of AgCN photocatalysts for photocatalytic elimination reaction.

Furthermore, we performed DFT calculation to study the effect of Ag introduction on the electronic structure of AgCN. The atomic
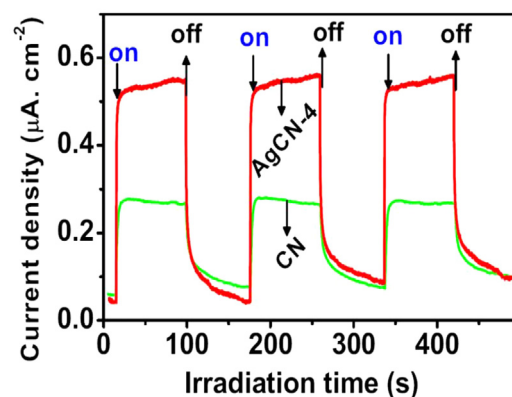
structure model of a perfect CN consisting of melon units is given in Fig. 6. Previous and our studies revealed that heteroatom preferentially substituted for the N atom of CN, and here the groups of periodic nitrogen atoms exist in the melon units, as marked with 1 and 2. From the calculations of the two models, it can be seen that the energy gap between the highest occupied molecular orbital (HOMO) and the lowest unoccupied molecular orbital (LUMO) was decreased from 1.96 eV (CN) to 0.38 (AgCN), and 1.44 eV (iso-AgCN). It is worth noting that HOMO levels present downshift for the cases of site 1 & 2 substitution, which is in best agreement with the experimental results. However, Gibbs free energy of Ag for replacing N of the AgCN and iso-AgCN was calculated to be −2092.16, and −2092.00 hartree, respectively, and the difference energy between AgCN and iso-AgCN is −96.72 kcal/mol. Therefore, AgCN mode should more fit our investigation, which will favor the investigation of photocatalytic methyl orange elimination over AgCN samples.

3.3. Photocatalytic activity

The Photocatalytic activity over AgCN for MO elimination was evaluated under visible-light irradiation at ambient temperature (Fig. 7). In dark environment for 120 min, MO concentration shows slight decrease over AgCN samples, and kept constant after 60 min, presenting the mere adsorption-desorption equilibrium between organic pollutant and AgCN samples. When the photocatalytic elimination of MO over the AgCN was carried out under the light irradiation, MO concentration decreased obviously, indicating that MO was photocatalytically eliminated over AgCN photocatalysts. From the performance profiles, there is a big difference in the elimination efficiency of AgCN photocatalysts, MO elimination efficiency is 38%, 54%, 66%, 81%, and 86%, corresponding to CN, AgCN-1,
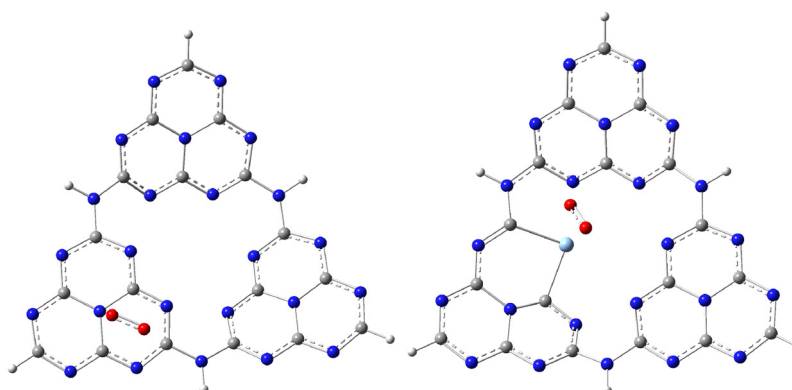

Fig. 11. The adsorption energy of O_2 on the CN (A) and AgCN (B).

AgCN-2, AgCN-3, AgCN-4, respectively, at 20 min of photocatalytic elimination reaction. Moreover, photooxidation reaction rate with using pseudo-first-order kinetic equation is 0.04, 0.06, 0.08, 0.10, and 0.13 min^{-1}, respectively. Particularly, k value of AgCN-4 is 3.25 times that of CN, meanwhile, we confirmed that introduction of Ag with excessive amount can not as always enhance the photocatalytic performance of AgCN photocatalysts compared with AgCN-4 (Fig. S3 & S4 of Supplementary material). Thus, introduction of Ag with moderate content can obviously promote the photocatalytic performance of CN for photocatalytic elimination of pollutants.

To further evaluate photoreactivity of AgCN, well-known Ag and/or Bi-based photocatalytic materials, (Bi$_2$WO$_6$ [15], BiOCl [31], Ag/CN (Ag loading is 0.5 at.%) [37], and Ag$_2$CO$_3$ [62]) were prepared according to references and used as photocatalysts for MO pollutant removal, the results are shown in Fig. 8. From the reaction efficiency, AgCN-4 photocatalyst shows higher photocatalytic performance compared with these photocatalysts, i.e., photocatalytic activity of AgCN-4 photocatalyst is 6.50, 8.13, 2.60, and 4.33 times that of Bi$_2$WO$_6$ (0.02 min^{-1}), BiOCl (0.016 min^{-1}), Ag/CN (0.05 min^{-1}), and Ag$_2$CO$_3$ (0.03 min^{-1}). Therefore, besides the enhanced photocatalytic performance, AgCN photocatalysts with low cost should have more advantages for potential application in the field of pollutant elimination. The long-term stability of photocatalysts in the photocatalysis process is very important for practical application. The cyclic utilization test results of MO photocatalytic elimination over AgCN-4 were shown in Fig. 9. It is found that AgCN-4 can efficiently eliminate MO pollutant and maintain a stable and effective photocatalytic activity.

Clearly, the photocatalytic activity of CN can be substantially improved by introducing Ag. To better understand how Ag affect the photocatalytic activity of CN, we investigated the photophysical processes of CN and AgCN. In Fig. 5A, B, & C, Ag introduction narrowed the bandgap energy of CN with the tuned conduction band and valence band levels as well as an enhanced light-adsorption intensity and the produced Ag LSPR, and the results indicate that AgCN can absorb more solar energy to produce more photogenerated electrons and holes pairs [63], which contributed to the improvement of photoactivity of AgCN. In Fig. 5D, we can see that much weakened emission intensity, nevertheless, suggests a greatly decreased radiative recombination probability of photoexcited charge carriers in AgCN samples [54,64]. We further measured the transient photocurrent response, and the results were shown in Fig. 10. We can see the similar photocurrent patterns for CN and AgCN samples. When light irradiated photocatalysts, photocurrent value quickly increased, nevertheless the current rapidly decreased to zero by switching off light, indicating photogenerated electrons transferred and contacted to form photocurrent, moreover, high photocurrent value represents efficient electron-holes separation and transportation [54,65,66]. Clearly, AgCN shows higher electron-holes separation and transportation efficiency than CN. Since O$_2$ is favorable for capturing photogenerated electrons to yield active oxygen species [67,68], O$_2$ adsorption and electron transfer capability over AgCN are also the keys for enhancing photooxidation elimination performance. We performed DFT calculation to study the O$_2$ absorption on the CN and AgCN, and the results were shown in Fig. 11A&B. It can be seen that, O$_2$ adsorption on CN is end-on modes in Fig. 10, while the side-on mode can be achieved for O$_2$ adsorption on AgCN (Fig. 11). The adsorption energy is −11.9 and −25.2 kcal/mol for CN, and AgCN, respectively. With respect to CN, O$_2$ can be easier adsorbed on AgCN, and electrons can be facilely transferred from AgCN to O$_2$, which was also experimentally confirmed by O$_2$-stripping. In Fig. 12, the corresponding CV curve for CN and AgCN-4 photocatalysts shows a single peak in the first scan (solid line), whereas the peak disappears in the second scan (dashed line). This experimental phenomena indicates the dissocaition of O$_2$ adsorbed on the photocatalysts [21].
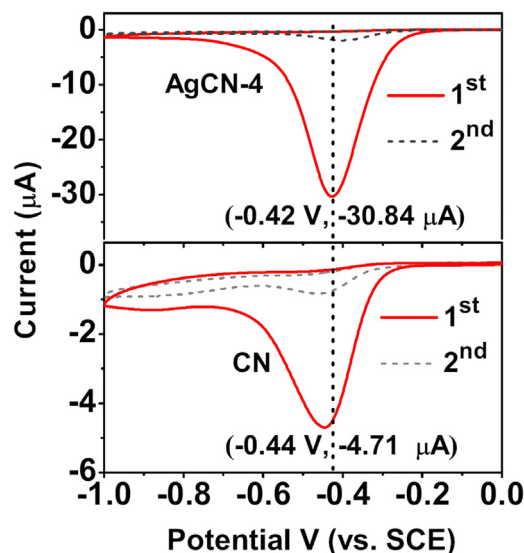

Fig. 12. CV curves of CN and AgCN-4 samples in 0.1 M NaOH aqueous solution with a scanning rate of 5 mV s^{-1}. Solid and dashed lines represent the first and second scans, respectively.

The peak onset and peak potential shift positively, the current density enhances noticeably as well as peak area increase obviously for AgCN-4, suggesting that electron be efficiently transferred to more O$_2$ molecular over AgCN-4, which facilely promotes O$_2$ dissocaition.

For organic pollutant elimination reaction, photoelectrons of photocatalysts would transfer to O$_2$, promotes O$_2$ dissocaition and simultaneously yield reactive oxygen species (ROS). We used isopropanol (IPA, 0.02 M), p-benzoquinone (BZQ, 0.001 M), and triethanolamine (TEOA, 0.01 M) as scavengers to trap hydroxyl radicals (•OH), superoxide anion radicals (•O$_2^-$) and photogenerated holes (h$^+$), respectively. In Fig. 13, we can see that variety of photocatalytic performance over AgCN-4 was as ever obvious after addition of IPA, i.e., C/C_0 reduced from 94% to 16% at 25 min of irradiation, suggesting that hydroxyl radical is not the main ROS for MO elimination. By contrast, C/C_0 varied from 94% to 52% or 83% MO degradation over AgCN-4 when BZQ or TEOA was added as radical scavenger in the photocatalysis system, respectively, revealing that hole and superoxide anion radical are reactive species during MO phtocatalytic decomposition process. Thus, combined with the electron structure, photocatalytic performance as well as radical scavenger experiment, a possible mechanism was demonstrated in Fig. 14. Upon visible light irradiation, AgCN-4 can generate excited electron-hole pairs due to the narrowed band gap, the enhanced sunlight absorption as well as Ag LSPR. The introduction of Ag into AgCN-4 improved carrier mobility efficiency, and thus the photogenerated electrons rapidly transferred from the CB of AgCN to dopant Ag atom. As a result, hole on VB of AgCN-4 eliminated MO pollutant by direct oxidation, in the meantime photoelectrons of AgCN-4 were transferred to O$_2$ by the introduced Ag to yield •O$_2^-$ for MO pollutant decomposition. Moreover, plasmonic Ag on AgCN-4 is efficient for light absorption and scattering, and thus can form LSPR effect as reflected by collective oscillation of electron around plasmonic Ag, which obviously promotes photoelectron-hole secession, transportation, and utilization over AgCN-4.

4. Conclusions

We designed AgCN photocatalysts by introducing Ag into CN for the photooxidation elimination of MO pollutant. Compared with CN, and typical Ag-, Bi-based photocatalysts, AgCN photocatalysts showed high photocatalytic elimination efficiency of MO pollu-
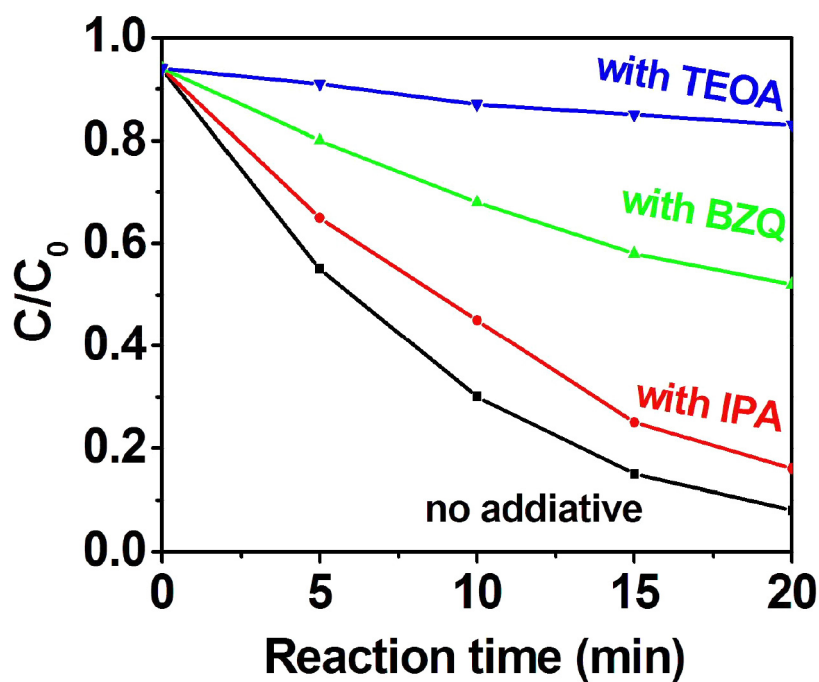
Fig. 13. The variation of MO concentration vs. illumination time for the AgCN sample, with the addition of triethanolamine (TEOA, 0.01 M), *p*-benzoquinone (BZQ, 0.001 M) and isopropanol (IPA, 0.02 M) as radical scavengers.
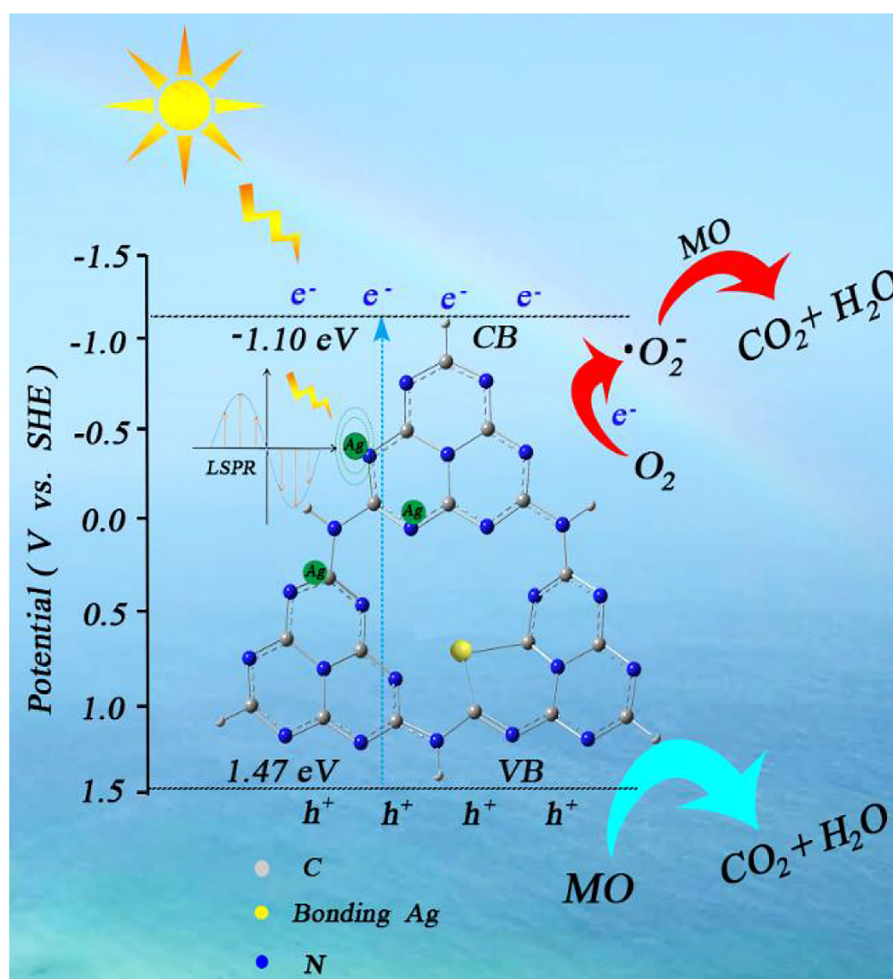
Fig. 14. Proposed photocatalytic mechanism for MO pollutant elimination over AgCN-4 photocatalyst.

tant under visible-light irradiation. The remarkable photocatalytic activity over AgCN photocatalysts is attributed to the sufficient sunlight absorption, efficient carrier mobility as well as enhanced O_2 adsorption state and amount. As confirmed by both experimental and theoretical perspectives, the results suggest that AgCN photocatalysts designed by introducing Ag into CN to weaken the planar hydrogen bonding would be an effective strategy to construct efficient visible-light-responsive photocatalysts for environmental purification.

Acknowledgments

Appendix A. Supplementary data

Supplementary data associated with this article can be found, in the online version, at http://dx.doi.org/10.1016/j.apcatb.2017.06.001.

References

[1] Y. Ma, X.L. Wang, Y.S. Jia, X.B. Chen, H.X. Han, C. Li, Chem. Rev. 114 (2014) 9987–10043.
[2] A.D. Paola, E. García-López, G. Marcì, L. Palmisano, J. Hazard. Mater. 211–212 (2012) 3–29.
[3] J.X. Low, B. Cheng, J.G. Yu, Appl. Surf. Sci. 392 (2017) 658–686.
[4] X. Li, J.G. Yu, M. Jaroniec, Chem. Soc. Rev. 45 (2016) 2603–2636.
[5] Y. Qu, W. Zhou, H.G. Fu, ChemCatChem 6 (2014) 265–270.
[6] Y. Qu, W. Zhou, Z.Y. Ren, C.G. Tian, J.L. Li, H.G. Fu, ChemPlusChem 79 (2014) 995–1000.
[7] J. Bian, Y. Qu, R. Fazal, X.L. Li, N. Sun, L.Q. Jiang, J. Phys. Chem. C 120 (2016) 11831–11836.
[8] A. Fujishima, X.T. Zhang, D.A. Tryk, Surf. Sci. Rep. 63 (2008) 515–582.
[9] P. Zhou, J.G. Yu, M. Jaroniec, Adv. Mater. 26 (2014) 4920–4935.
[10] Q.J. Xiang, J.G. Yu, M. Jaroniec, Chem. Soc. Rev. 41 (2012) 782–796.
[11] P.V. Kamat, J. Phys. Chem. Lett. 3 (2012) 663–672.
[12] T.F. Yeh, F.F. Chan, C.T. Hsieh, H. Teng, J. Phys. Chem. C 115 (2011) 22587–22597.
[13] T.F. Yeh, J.M. Syu, C. Cheng, T.H. Chang, H. Teng, Adv. Funct. Mater. 20 (2010) 2255–2262.
[14] L. Tang, J.J. Wang, G.M. Zeng, Y.N. Liu, Y.C. Deng, Y.Y. Zhou, J. Tang, J.J. Wang, Z. Guo, J. Hazard. Mater. 306 (2016) 295–304.
[15] J.X. Low, J.G. Yu, Q. Li, B. Cheng, Phys. Chem. Chem. Phys. 16 (2014) 1111–1120.
[16] J.J. Yang, D.M. Chen, Y. Zhu, Y.M. Zhang, Y.F. Zhu, Appl. Catal. B: Environ. 205 (2017) 228–237.
[17] H. Wang, Y.H. Liang, L. Liu, J.S. Hu, W.Q. Cui, Appl. Surf. Sci. 392 (2017) 51–60.
[18] O. Mehraj, B.M. Pirzada, N.A. Mir, M.Z. Khan, S. Sabir, Appl. Surf. Sci. 387 (2016) 642–651.
[19] G.Y. Rao, Q.Y. Zhang, H.L. Zhao, J.T. Chen, Y. Li, Chem. Eng. J. 302 (2016) 633–640.
[20] P. Zhang, X.Y. Yang, Z.B. Zhao, B.B. Li, J.Z. Gui, D. Liu, J.S. Qiu, Carbon 116 (2017) 59–67.
[21] L.M. He, L.Q. Jing, Y.B. Luan, L. Wang, H.G. Fu, ACS Catal. 4 (2014) 990–998.
[22] L.M. Song, J.F. Yang, S.J. Zhang, Chem. Eng. J. 309 (2017) 222–229.
[23] Y.L. Zhang, C.R. Xie, F.L. Gu, H.H. Wu, Q. Guo, J. Hazard. Mater. 315 (2016) 23–34.
[24] J.W. Li, X.J. Ji, X. Li, X.H. Hu, Y.F. Sun, J.J. Ma, G.W. Qiao, Appl. Surf. Sci. 372 (2016) 30–35.
[25] Y. Xie, Z.H. Huang, Z.J. Zhang, X.G. Zhang, R.L. Wen, Y.G. Liu, M.H. Fang, X.W. Wu, Appl. Surf. Sci. 389 (2016) 56–66.
[26] H.G. Yu, G.Q. Cao, F. Chen, X.F. Wang, J.G. Yu, M. Lei, Appl. Catal. B: Environ. 160–161 (2014) 658–665.
[27] Y.Y. Bu, Z.Y. Chen, ACS Appl. Mater. Interfaces 6 (2014) 17589–17598.
[28] B. Chai, J. Li, Q. Xu, Ind. Eng. Chem. Res. 53 (2014) 8744–8752.
[29] S. Zhao, Y.W. Zhang, Y.M. Zhou, C. Zhang, X.L. Sheng, J.S. Fang, M.Y. Zhang, ACS Sustain. Chem. Eng. 5 (2017) 1416–1424.
[30] Y.F. Zhang, M. Park, H.Y. Kim, B. Ding, S.J. Park, Appl. Surf. Sci. 384 (2016) 192–199.
[31] M. Li, H.W. Huang, S.X. Yu, N. Tian, F. Dong, X. Du, Y.H. Zhang, Appl. Surf. Sci. 386 (2016) 285–295.
[32] W.J. Ong, L.L. Tan, Y.H. Ng, S.T. Yong, S.P. Chai, Chem. Rev. 116 (2016) 7159–7329.
[33] X.C. Wang, K. Maeda, A. Thomas, K. Takanabe, G. Xin, J.M. Carlsson, K. Domen, M. Antonietti, Nat. Mater. 8 (2009) 76–80.
[34] Y.F. Li, R.X. Jin, X. Fang, Y. Yang, M. Yang, X.C. Liu, Y. Xing, S.Y. Song, J. Hazard. Mater. 313 (2016) 219–228.
[35] T.F. Xu, D.J. Ni, X. Chen, F. Wu, P.F. Ge, W.Y. Lu, H.G. Hu, Z.X. Zhu, W.X. Chen, J. Hazard. Mater. 317 (2016) 17–26.
[36] G.H. Dong, L.P. Yang, F. Wang, L. Zang, C.Y. Wang, ACS Catal. 6 (2016) 6511–6519.
[37] O. Fontelles-Carceller, M.J. Muñoz-Batista, M. Fernández-García, A. Kubacka, ACS Appl. Mater. Interfaces 8 (2016) 2617–2627.
[38] L.H. Lin, H.H. Ou, Y.F. Zhang, X.C. Wang, ACS Catal. 6 (2016) 3921–3931.
[39] Y. Chen, B. Lin, H. Wang, Y. Yang, H.B. Zhu, W.L. Yu, J.M. Basset, Chem. Eng. J. 286 (2016) 339–346.
[40] S.W. Cao, J.G. Yu, J. Phys. Chem. Lett. 5 (2014) 2101–2107.
[41] P. Niu, G. Liu, H.M. Cheng, J. Phys. Chem. C 116 (2012) 11013–11018.
[42] P. Niu, Y.Q. Yang, J.C. Yu, G. Liu, H.M. Cheng, Chem. Commun. 50 (2014) 10837–10840.
[43] Q. Han, B. Wang, J. Gao, Z.H. Cheng, Y. Zhao, Z.P. Zhang, L.T. Qu, ACS Nano 10 (2016) 2745–2751.
[44] S.W. Cao, J.X. Low, J.G. Yu, M. Jaroniec, Adv. Mater. 27 (2015) 2150–2176.
[45] B.V. Lotsch, M. Doblinger, J. Sehnert, L. Seyfarth, J. Senker, O. Oeckler, W. Schnick, Chem. Eur. J. 13 (2007) 4969–4980.
[46] P. Niu, L.L. Zhang, G. Liu, H.M. Cheng, Adv. Mater. 22 (2012) 4763–4770.
[47] S.B. Yang, Y.J. Gong, J.S. Zhang, L. Zhan, L.L. Ma, Z.Y. Fang, R. Vajtai, X.C. Wang, P.M. Ajayan, Adv. Mater. 25 (2013) 2452–2456.
[48] N. Sagara, S. Kamimura, T. Tsubota, T. Ohno, Appl. Catal. B: Environ. 192 (2016) 193–198.
[49] Y.R. Guo, T.X. Chen, Q. Liu, Z.G. Zhang, X.M. Fang, J. Phys. Chem. C 120 (2016) 25328–25337.
[50] X.G. Ma, Y.H. Lv, J. Xu, Y.F. Liu, R.Q. Zhang, Y.F. Zhu, J. Phys. Chem. C 116 (2012) 23485–23493.
[51] L. Ke, P.F. Li, X. Wu, S.J. Jiang, M.B. Luo, Y.H. Liu, Z.G. Le, C.Z. Sun, S.Q. Song, Appl. Catal. B: Environ. 205 (2017) 319–326.
[52] Z. Li, C. Kong, G.X. Lu, J. Phys. Chem. C 120 (2016) 56–63.
[53] F. Bonaccorso, Z. Sun, T. Hasan, A.C. Ferrari, Nat. Photon. 4 (2010) 611–622.
[54] K. Wang, Q. Li, B.S. Liu, B. Cheng, W.K. Ho, J.G. Yu, Appl. Catal. B: Environ. 176–177 (2015) 44–52.
[55] Q. Huang, J.G. Yu, S.W. Cao, C. Cui, B. Cheng, Appl. Surf. Sci. 358 (2015) 350–355.
[56] B.C. Zhu, P.F. Xia, Y. Li, W.K. Ho, J.G. Yu, Appl. Surf. Sci. 391 (2017) 175–183.
[57] X.J. She, H. Xu, Y.G. Xu, J. Yan, J.J. Xia, Y.H. Song, Y. Jiang, Q. Zhang, H.M.J. Li, Mater. Chem. A 2 (2014) 2563–2570.
[58] P.K. Chuang, K.H. Wu, T.F. Yeh, H. Teng, ACS Sustain. Chem. Eng. 4 (2016) 5989–5997.
[59] C.Y. Liu, Y.H. Zhang, F. Dong, X. Du, H.W. Huang, J. Phys. Chem. C 120 (2016) 10381–10389.
[60] T.R. Wu, H.L. Shen, L. Sun, B. Cheng, B. Liu, J.C. Shen, ACS Appl. Mater. Interfaces 4 (2012) 2041–2047.
[61] D. Düzenli, J. Phys. Chem. C 120 (2016) 20149–20157.
[62] S.Q. Song, B. Cheng, N.S. Wu, A.Y. Meng, S.W. Cao, J.G. Yu, Appl. Catal. B: Environ. 181 (2016) 71–78.
[63] P. Zhang, T. Wang, X.X. Chang, J.L. Gong, Acc. Chem. Res. 49 (2016) 911–921.
[64] F. Raziq, Y. Qu, M. Humayun, A. Zada, H.T. Yu, L.Q. Jing, Appl. Catal. B: Environ. 201 (2017) 486–494.
[65] Z.J. Li, Y. Qu, K. Hu, M. Humayun, S.Y. Chen, L.Q. Jing, Appl. Catal. B: Environ. 203 (2017) 355–362.
[66] S.Q. Song, A.Y. Meng, S.J. Jiang, B. Cheng, C.J. Jiang, Appl. Surf. Sci. 396 (2017) 1368–1374.
[67] N. Waiskopf, Y. Ben-Shahar, M. Galchenko, I. Carmel, G. Moshitzky, H. Soreq, U. Banin, Nano Lett. 16 (2016) 4266–4273.
[68] H. Zhang, L.H. Guo, L.X. Zhao, B. Wan, Y. Yang, J. Phys. Chem. Lett. 6 (2015) 958–963.